Analysis of difference-frequency wave loads and quadratic transfer functions on a restrained semi-submersible floating wind turbine

Haoran Li [a],[*], Erin E. Bachynski-Polić [a],[b]

[a] *Department of Marine Technology, Norwegian University of Science and Technology (NTNU), Trondheim, Norway*
[b] *Centre for Autonomous Marine Operations and Systems (AMOS), NTNU, Trondheim, Norway*

ARTICLE INFO

ABSTRACT

One of the concerns regarding numerical simulation of floating wind turbines (FWTs) in waves is underprediction of resonant responses in the low-frequency range. In the present work, the difference-frequency wave loads on a restrained semi-submersible FWT subject to bichromatic waves are investigated by higher-fidelity tools (Computational Fluid Dynamics, CFD) and simplified engineering tools based on potential flow theory with Morison type drag. The effects of mean pitch angle (trim) and the wave force distribution on the multimember semisubmersible are assessed. Compared to the CFD results, wave loads estimated by engineering models are in good agreement at the wave frequencies, while slightly larger differences occur at the surge and pitch natural frequencies. The most significant underprediction of the surge force at the surge natural frequency occurs in the heave plate of the floater. Compared to the upright floater, the increased wave loads on the trimmed floater at the surge natural frequency are more significant than those at the pitch natural frequency. Furthermore, quadratic transfer functions (QTFs) are estimated based on the CFD model with a set of bichromatic wave cases. A new approach is found to use the CFD results to modify the QTFs in lower-fidelity engineering tools. This approach is validated against experimental measurements in irregular waves. Good agreement is achieved between measured and numerically estimated difference-frequency wave loads by engineering tools with modified QTFs.

1. Introduction

Floating wind turbines (FWTs) can harness the energy from winds over deep water and farther offshore. However, this technology is still at an early stage of development. Well-validated modelling tools are needed to capture highly nonlinear wave loads on the floater induced by the harsh environments and steep waves. In this paper, the focus is on a semi-submersible FWT.

The international collaboration projects known as OC4 (Phase II) and OC5 (Phase II) verified and validated semi-submersible FWT modelling tools through code-to-code and code-to-data comparisons. Larger differences between simulated loads/motions and measurements were seen in the low-frequency domain (Robertson et al. 2014, 2017). Although the low-frequency wave exciting loads are small, these loads can result in large motions due to resonant responses in surge and pitch. Accurate estimation of difference-frequency wave loads is therefore important for capturing global responses (Coulling et al., 2013). Other investigations (Bachynski et al., 2016; Berthelsen et al., 2016; Luan et al., 2016) have

similar findings as the OC4 projects: the predictions of low-frequency motions were very sensitive to the viscous drag coefficients on the columns and pontoons.

Given that engineering tools based on first- and second- order potential flow theory with or without Morison-type drag limit hydrodynamic modelling to linear or weakly nonlinear models and generally underpredict the highly nonlinear difference-frequency wave loads, it is reasonable to consider higher-fidelity modelling tools that account for the fully nonlinear terms of the Navier-stokes equations, such as computational fluid dynamics (CFD). CFD has been shown to improve predictions of nonlinear wave loads and motions of semi-submersible FWTs, such as capturing shadowing effects and transverse forces from vortex shedding and nonlinear phenomena in steep wave conditions (Benitz et al. 2014, 2015; Hu et al., 2014; Liu and Hu, 2014; River-a-Arreba et al., 2019). Ideally, one would like to carry out irregular wave simulations to study the difference-frequency loads. However, the substantial computational time of CFD tools makes it difficult to carry out long simulations of irregular waves, and CFD simulations of irregular
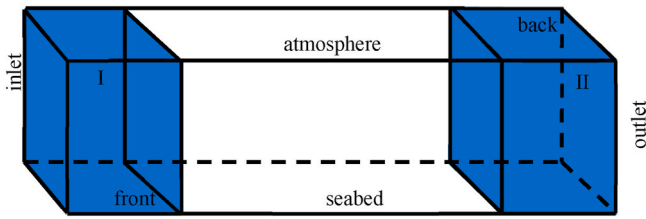
Fig. 1. Schematic representation of computational domain.

waves may suffer from significant wave damping triggered by an increase in the viscosity around the air-water interface (Devolder et al., 2017). Therefore, bichromatic waves are applied to study the difference-frequency wave loads and quadratic transfer functions (QTFs) in this paper. Modified QTFs based on the CFD results are validated against experimental results in irregular waves.

Bichromatic waves have also been used to examine the difference-frequency wave loads and motions of floating systems by other researchers. Pessoa and Fonseca (Pessoa et al., 2010; Fonseca et al., 2011; Pessoa and Fonseca, 2015) investigated the slowly-varying wave exciting forces and motions of a body with a simple geometry in bichromatic waves experimentally and numerically. The numerical models were able to qualitatively represent the measured slowly-varying forces, namely the order of magnitude of the forces, the tendencies along the mean wave period range and the increase with the decreasing water depth. Ohyama and Hsu (1995) examined the slow sway motion of a rectangular body in response to bichromatic waves and found the second-order approximation was applicable in a small-amplitude range. Lopez-Pavon et al. (2015) measured second-order loads on a semi-submersible FWT directly in biochromatic waves and found full QTFs instead of Newman's approximation should be implemented for accurate estimation of difference-frequency wave loads. Simos et al. (2018) investigated the second-order hydrodynamics of a semisubmersible FWT in bichromatic waves, and the measured results matched well with the numerical estimations by QTFs.

The focus of present study, which is inspired by the ongoing Offshore Code Comparison Collaboration, Continued, with Correlation, and unCertainty (OC6) project (Wang et al., 2021), is on the investigation of nonlinear difference-frequency wave loads on a restrained semi-submersible FWT subjected to bichromatic waves by CFD and engineering tools. The bichromatic waves are generated by adding together two regular waves at different frequencies whose difference coincides with either the surge or pitch natural frequency of the FWT. A trimmed floater is additionally modelled to examine the change of wave loads due to trim induced by the mean aerodynamic thrust force. Meanwhile, wave loads on individual columns are extracted to better understand how the nonlinear wave loads change among the different components of semi-submersible FWTs.

In order to be able to use the CFD results in practical simulations, the difference-frequency wave loads from the bichromatic waves are used to modify the QTFs calculated using potential flow theory. Finally, the modified QTFs in the engineering tools are validated by comparing the numerically estimated difference-frequency wave loads in irregular waves against experimental measurements. The experimental measurements of wave loads on the restrained semi-submersible FWT are from Phase I of the OC6 project (Robertson et al., 2020). An irregular wave with significant wave height $H_s = 7.1$ m and peak period $T_p = 12.1$ s, following the JONSWAP wave spectrum with peak enhancement factor equal to 3.3, is considered. All data and results are given at full scale.

Sections 2 and 3 describe the CFD and potential flow theory models, respectively. The approaches for estimating and modifying the QTFs are described in Section. 4. In Section 5, comparisons of wave exciting loads on the upright and trimmed semi-submersible FWT by CFD and engineering tools are shown first, followed by the estimations and modifications of QTFs in bichromatic waves and the validations in irregular waves. The conclusions are presented in Sec. 6.

2. Computational fluid dynamics (CFD) model

The multiphase interFoam solver in OpenFOAM (Weller et al., 1998) is a fully nonlinear Navier-Stokes/Volume-Of-Fluid (VOF) solver which can accurately simulate complex free surface flows and fluid-structure interaction. Extending the interFoam solver with the implementation of the wave generation and absorption toolbox, waves2Foam, developed by Jacobsen et al. (2012), generates the waveFoam solver used
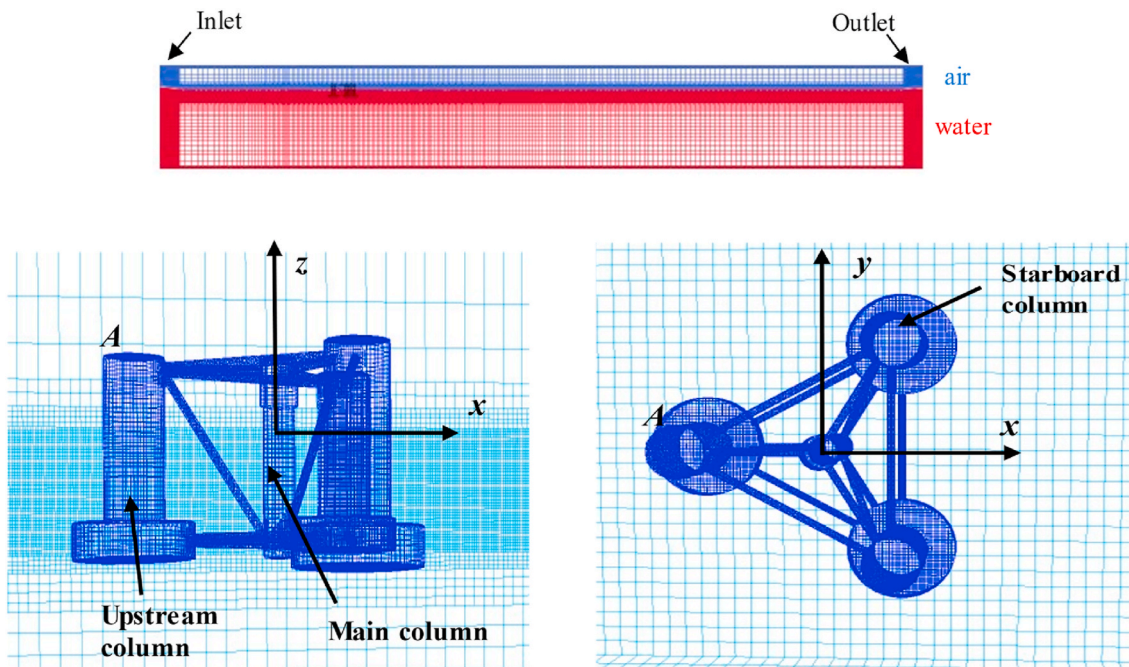

Fig. 2. The computational domain (top) and mesh around floater of wind turbine (bottom) in the CFD simulations.

Table 1
Bichromatic wave parameters (full scale).

$df = 0.01$ Hz (Surge natural frequency)				
Wave index	T1 (s)	T2 (s)	A1 (m)	A2 (m)
S1	20	16.81	1.67	1.79
S2	16.67	14.39	1.79	1.74
S3	14.29	12.58	1.74	1.74
S4	13.33	11.83	1.74	1.73
S5	12.50	11.17	1.73	1.71
S6	11.87	10.58	1.57	1.26
S7	11.11	10.05	1.50	1.50
S8	10.53	9.57	0.94	0.64
S9	10.00	9.13	0.84	0.54
S10	8.33	7.72	0.31	0.21
S11	7.14	6.69	0.22	0.16
S12	6.67	6.27	0.17	0.12

$df = 0.032$ Hz (Pitch natural frequency)				
Wave index	T1 (s)	T2 (s)	A1 (m)	A2 (m)
P1	20	12.20	1.67	1.74
P2	16.67	10.87	1.79	1.73
P3	14.29	9.80	1.74	1.70
P4	13.33	9.35	1.74	1.66
P5	12.50	8.93	1.50	1.50
P6	11.87	8.55	1.59	0.86
P7	11.11	8.20	1.44	0.76
P8	10.53	7.87	1.28	0.70
P9	10.00	7.58	1.13	0.64
P10	8.33	6.58	0.41	0.19
P11	7.14	5.81	0.22	0.12
P12	6.67	5.50	0.18	0.10

throughout the current work.

2.1. Governing equations

The governing equations are the two-phase incompressible RANS equations, consisting of a mass conservation and a momentum conservation equation for an incompressible flow of air and water, expressed as:

$$\frac{\partial u_i}{\partial x_i} = 0 \tag{1}$$

$$\frac{\partial \rho u_i}{\partial t} + \frac{\partial \rho u_j u_i}{\partial x_j} = -\frac{\partial p^*}{\partial x_i} + F_{b,i} + \frac{\partial}{\partial x_j}\left[\mu_{eff}\frac{\partial u_i}{\partial x_j}\right] \tag{2}$$

where u_i $(i = x, y, z)$ are the fluid velocity in Cartesian coordinates, ρ is the fluid density, p^* is pressure in excess of the hydrostatic pressure, F_b is an external body force including gravity and μ_{eff} is the effective dynamic viscosity.

Furthermore, in the VOF method, the local density ρ within a computational cell is given by water volume fraction α. The effective dynamic viscosity μ_{eff} is calculated by combining a weighted value based on the volume fraction α with the additional turbulent dynamic viscosity $\rho\nu_t$.

$$\rho = \alpha\rho_{water} + (1-\alpha)\rho_{air} \tag{3}$$

$$\mu_{eff} = \alpha\mu_{water} + (1-\alpha)\mu_{air} + \rho\nu_t \tag{4}$$

where α is one for water, zero for air, and in between zero and one for all intermediate values.

The VOF method (Hirt and Nichols, 1981) is used to track the air-water interface. The volume fraction α is advanced in time once the velocity is found by Eqs. (1) and (2), following an advection equation (Eq. (5)).

$$\frac{\partial \alpha}{\partial t} + \frac{\partial u_i \alpha}{\partial x_i} + \frac{\partial u_{r,i}\alpha(1-\alpha)}{\partial x_i} = 0 \tag{5}$$

Using a standard finite-volume approximation for solving Eq. (5) will lead to significant smearing of the interface. The last term on the left-hand side of Eq. (5) is introduced as an interface compression term (Berberović et al., 2009). It is only active in the vicinity of the interface, $0 < \alpha < 1$. To ensure the stability of the solution, a multi-dimensional flux limited scheme (MULES) is applied.

To identify the free surface elevation, the volume fraction α is integrated over a vertical line around the air-water interface in the waves2Foam package.

2.2. Turbulence model

Turbulent effects are incorporated in the governing equations by using different transport equations to calculate the turbulent kinematic viscosity. The $k - \omega$ SST turbulence model (Menter et al., 2003), a blending of the $k - \omega$ (Wilcox, 1998) and the $k - \varepsilon$ (Launder and Spalding, 1983) models, has shown good results for simulating two-phase flow and predicting wave elevation (Rahman et al., 2007, Brown et al., 2014) and is applied in this paper. The equations for the incompressible $k - \omega$ SST turbulence model for a single fluid in Open-Foam are given as:

$$\frac{\partial k}{\partial t} + \frac{\partial u_j k}{\partial x_j} - \frac{\partial}{\partial x_j}\left[(\nu + \sigma_k\nu_t)\frac{\partial k}{\partial x_j}\right] = P_k - \beta^*\omega k \tag{6}$$

$$\frac{\partial \omega}{\partial k} + \frac{\partial u_j\omega}{\partial x_j} - \frac{\partial}{\partial x_j}\left[(\nu + \sigma_\omega\nu_t)\frac{\partial \omega}{\partial x_j}\right] = \frac{\gamma}{\nu_t}G - \beta\omega^2 + 2(1-F_1)\frac{\sigma_{\omega 2}}{\omega}\frac{\partial k}{\partial x_j}\frac{\partial \omega}{\partial x_j} \tag{7}$$

where k is the turbulent kinetic energy, and P_k is the production term of k. ν is the kinematic viscosity, ν_t is the turbulent kinematic viscosity, and ω is the specific dissipation rate. See Menter et al. (2003) for details. In the present work, in order to avoid excessive wave damping due to the increased viscosity around the air-water interface (Devolder et al., 2017; Fan and Anglart, 2020), a modified waveFoam solver is built to explicitly consider the density in the incompressible $k - \omega$ SST model (Fan and Anglart, 2020).

2.3. Boundary conditions

To solve the governing equations of the Navier-Stokes/VOF solver, boundary conditions are imposed to all the surfaces in the numerical domain. The general denomination of boundary surfaces is given in Fig. 1.

- The velocity and the α field at the inlet are given by the applied wave theory. Here, second order bichromatic wave theory (Madsen and Fuhrman, 2006) is used. The parameters of bichromatic waves are described in Table 1. The pressure is specified as zero normal gradient at the inlet boundary. k is fixed at zero and ω is set as 0.001 1/s.
- At the outlet, all the boundaries are specified as zero normal gradient.
- On the floater surface, a no-slip boundary condition (zero velocity) is specified, and the pressure is set as zero normal gradient. k is fixed at 1e-5 m^2/s^2 and ω is set as 1.0 1/s.
- For the atmosphere, the total pressure is set as zero and an atmospheric boundary condition is set for the velocity and the α field. This means that air and water are allowed to leave the numerical domain, while only air is allowed to flow back in. k is fixed at zero and ω is specified as zero normal gradient.
- At the front, back and bottom, all the conditions are set as zero normal condition.
- A continuous wall function based on Spadling's law (Dudley Brian, 1961) switching between low and high Reynolds numbers is implemented for the turbulent viscosity. Hence, it requires that the non-dimensional wall distance y^+ should be between 10 and 300.

Table 2

Mesh convergence studies, P5 (Time step = 0.001414 s).

Cell size	Frequency (Hz)	Analytical solution	Level 2	Error (%)	Level 3	Error (%)	Level 4	Error (%)
			0.03 m		0.015 m		0.0075 m	
Wave (m)	0.08	1.501	1.488	0.87	1.495	0.40	1.497	0.27
	0.112	1.498	1.442	3.74	1.475	1.54	1.489	0.60
	0.032	0.0257	0.0310	20.74	0.0268	4.20	0.0261	1.39
Surge force (KN)	0.08	–	6691	3.54	6804	1.92	6937	–
	0.112	–	5749	3.33	5903	0.74	5947	–
	0.032	–	56.46	9.79	59.95	4.22	62.59	–
Pitch moment (MNm)	0.08	–	89.35	1.54	90.37	0.42	90.75	–
	0.112	–	112.2	3.11	114.4	1.21	115.8	–
	0.032	–	5.921	8.38	5.648	3.39	5.463	–

For the modified waveFoam solver, the bichromatic wave elevation will decrease at the end of simulation if a uniform turbulent viscosity is implemented. Different values of the turbulent kinetic energy (k) and specific dissipation rate (ω) at the inlet and floater surface are applied to accurately simulate the flow around the floater while reducing the wave damping.

The bichromatic waves considered here are chosen such that the first order components are around the peak periods (12.1 s) of the irregular wave event, and the difference frequency aligns with either the surge (S) or pitch (P) natural frequency where the largest wave-induced responses can be excited in irregular waves. The desired wave amplitude (approximately 1.75 m) was selected such that the calculated maximum wave height when two waves are added linearly is close to the significant wave height of the irregular-wave spectrum (7.1 m) (Tom et al., 2019). However, for shorter wave periods, the same wave amplitude results in steeper waves and increased viscosity around the air-water interface. As a result, the generated wave elevation in the CFD simulation attenuates over the time. To avoid excessive attenuation, smaller wave heights are applied for the shorter wave periods.

2.4. Relaxation zones

The relaxation zones (blue part in Fig. 1) in the waves2Foam toolbox (Jacobsen et al., 2012) are implemented to avoid wave reflection from outlet boundary (II) and also to prevent internally reflected waves (I). Rectangular relaxation zones are defined in this work. See Bruinsma's work (2018) for details.

2.5. Computational domain

The floater at scale 1:50 was built in the CFD simulations based on the OC5-DeepCwind floating wind system (Robertson et al., 2016). The right-handed coordinate system originates at the center of the main column at the still water line, with positive x being in the direction of propagating waves, and z being up, as shown in Fig. 2. The width (3.72 m) and water depth (3.6 m) of the numerical wave tank are equal to those of the experimental facility. The same length (36 m) as one in the

previous study (Li and Bachynski, 2021) is implemented to ensure the reflected waves are dissipated thoroughly. In addition, the height of the air regime is set to 1 m. Fig. 2 shows the numerical wave tank and floater.

2.6. Spatial and temporal discretization

OpenFOAM is based on finite volume discretization. The computational domain is discretized into finite regions in space known as cells. The size of a cell in all the directions is 0.12 m after discretization. Thereafter, for the wave generating regime and the floater surface, the mesh is refined. Mesh convergence studies for different mesh levels with 0.001414 s time step (Table 2) were carried out by comparing the wave elevations and calculated wave loads at wave- and difference-frequencies for wave P5. The analytical solutions of wave are calculated from second-order bichromatic wave theory (Marthinsen and Winterstein, 1992). The errors in wave elevations are shown relative to the analytical solutions while the wave loads are compared to those with the finest mesh size (Level 4).

Globally, the 3-3 level of refinement with 4-4 refinement locally around the cross braces is applied in subsequent simulations. In addition, 25 cell layers adjacent to the floater surface are generated for the turbulence modelling. The thickness of the first layer is 2.0 μm and its expansion ratio is 1.2. The local refinement allows for a high-resolution interface while keeping the total number of computational cells (around 17 million) relatively low.

In order to ensure numerical stability, the Courant-Friedrichs-Lewy (CFL) condition is implemented to determine the time step. Different fixed time steps with the 3-3 level of mesh refinement are chosen to carry out the time step convergence study of the wave elevations and calculated wave loads for wave P5 and shown in Table 3. All the results are obtained through the same method as the mesh convergence studies. Considering the computational time, 'time step 3' is used in this work.

The wave loads at the limit of infinite temporal and spatial resolution are calculated based on the Richardson extrapolation with the standard power-law error estimator (Eça and Hoekstra, 2014). The resulting apparent order of convergence if found to be 2. The discretization

Table 3

Time step convergence study, P5 (same spatial discretization, Level 3).

	Frequency (Hz)	Analytical solution (m)	Time step 1 (m)	Error (%)	Time step 2 (m)	Error (%)	Time step 3 (m)	Error (%)	Time step 4 (m)	Error (%)
Time step (s)			7.07E-3		2.828E-3		1.414E-3		7.07E-4	
Wave (m)	0.08	1.501	1.463	2.53	1.49	0.73	1.495	0.40	1.496	0.33
	0.112	1.498	1.385	7.54	1.453	3.00	1.475	1.54	1.491	0.47
	0.032	0.0257	0.0327	27.2	0.0298	16.1	0.0268	4.20	0.0261	1.56
Surge force (KN)	0.08	–	6703	3.57	6783	2.08	6804	1.78	6927	–
	0.112	–	5797	2.67	5866	1.51	5903	0.89	5956	–
	0.032	–	55.36	9.11	58.49	3.97	59.95	1.58	60.91	–
Pitch moment (MNm)	0.08	–	89.50	1.15	90.17	0.41	90.37	0.19	90.54	–
	0.112	–	112.1	3.03	113.4	1.90	114.4	1.04	115.6	–
	0.032	–	6.074	8.81	5.761	3.21	5.648	1.18	5.582	–

Table 4

Estimated uncertainties in the CFD simulations.

	Difference frequency 0.032 Hz	First wave frequency 0.08 Hz	Second wave frequency 0.112 Hz
Wave elevation	4.2%	0.40%	1.54%
Surge force	8.11%	3.99%	2.14%
Pitch moment	6.69%	0.78%	2.99%

Table 5

Overview of different settings in SIMA.

Label	Load model
SIMA1/ Linear1	Only linear potential flow theory
SIMA2/ Linear2	SIMA1/Linear1 with original quadratic transfer function (QTF) from WAMIT
SIMA3/ Linear3	SIMA 2/Linear2 with integration of Morison drag force to mean free surface
SIMA4/ Linear4	SIMA 2/Linear2 with integration of Morison drag force to the undisturbed linear free surface
SIMA5/ Linear5	SIMA 4/Linear4 with consideration of axial drag force on the heave plates
SIMA6	SIMA5 with replacement of the original QTF from WAMIT with modified QTF from CFD

uncertainty of wave loads is identified as the estimated discretization error multiplied by a suitable safety factor of 1.25 (Eça and Hoekstra, 2006). The total uncertainty of wave loads is calculated by combining the temporal and spatial discretization uncertainties in the root-sum-of-squares fashion. The uncertainty in the incident wave amplitude is defined as the discretization error of the selected mesh size and time step relative to the analytical solution. The results are shown in Table 4. The uncertainties in the difference-frequency components tend to be much larger than those at the wave frequencies, especially for the wave elevation.

3. Potential flow theory model

A numerical model based on potential flow theory is built in SIMA (SIMO-RIFLEX), developed by SINTEF Ocean. SIMA is a state-of-the-art time-domain code that can address both the hydrodynamic loads (SIMO (MARINTEK, 2012)) and the structural dynamic problem (RIFLEX (Ormberg and Passano, 2012)) in a fully coupled way and has been used to study numerous types of floating wind turbines.

In present simulations, only the floater of the wind turbine is modelled. The frequency-dependent hydrodynamic properties, such as first-order potential flow forces and QTFs, are estimated based on potential flow theory (WAMIT (Lee, 1995)) or modified based on the CFD simulations and subsequently input to SIMA. The viscous forces on the columns and cross braces of the floater are considered by including the drag forces from Morison's equation. A constant transverse drag coefficient (0.744 based on towing tests (Robertson et al., 2020)) is applied for each component of the floater. Additionally, the axial drag force for the heave plate is calculated based on Eq. (8), where D is the diameter of the heave plate and U is the axial wave velocity. Here, the axial drag coefficient $C_{da} = 2.48$ based on previous comparisons of a similar engineering tool with experimental data from the DeepCwind test campaign (Robertson et al., 2014).

$$F_{DA} = \frac{1}{2}\rho C_{da} \frac{\pi D^2}{4} U|U| \qquad (8)$$

In the potential flow theory model, different force contributions are investigated, as summarized in Table 5. For simulations referred to as 'SIMA', the generated (nonlinear) wave elevation from CFD is used as an input, while simulations indicated as 'Linear' take a time series based on

the first-order bichromatic theory (a simple linear super-position of sine signals) as input. All simulations are carried out in the SIMA software. In both cases, when a wave signal is input into the SIMA software, it is treated as a superposition of linear regular waves at different frequencies, and all the components are assumed to travel in the positive x-direction. Additionally, the time series of bichromatic waves are input into SIMA software by a high-pass filter with a 0.008 Hz cut-off frequency for all simulations in the current work. The difference between 'SIMA' and 'Linear' can be seen in the bottom subplot of Fig. 4. The comparisons of 'SIMA' and 'Linear' models are used to investigate the effects of nonlinear wave component on the wave- and difference-frequency wave loads.

4. QTF estimation and modification

4.1. Analysis of the numerical data

The harmonic components (mean values and all first- and second-order harmonics) of wave elevation and wave loads are identified by fitting a second order expansion model to the steady-state part of the numerical time signal with a least squares procedure. In bichromatic waves, the wave elevations and wave loads are approximated by Eq. (9). Components above the 2nd order are found to be negligible.

$$\begin{aligned} I(t) = & \bar{I} + I_1^{c(1)}\cos(\omega_1 t) + I_1^{s(1)}\sin(\omega_1 t) + I_2^{c(1)}\cos(\omega_2 t) + I_2^{s(1)}\sin(\omega_2 t) \\ & + I_1^{c(2)}\cos(2\omega_1 t) + I_1^{s(2)}\sin(2\omega_1 t) + I_2^{c(2)}\cos(2\omega_2 t) + I_2^{s(2)}\sin(2\omega_2 t) \\ & + I^{c(+)}\cos\{(\omega_1 + \omega_2)t\} + I^{s(+)}\sin\{(\omega_1 + \omega_2)t\} \\ & + I^{c(-)}\cos\{(\omega_1 - \omega_2)t\} + I^{s(-)}\sin\{(\omega_1 - \omega_2)t\} \end{aligned}$$

(9)

In Eq. (9), I is the quantity of interest (the wave elevation η or wave loads F), and ω_1, ω_2 are the two incident wave frequencies. Each harmonic component is represented by a sum of cosine and sine parts, thus allowing the identification of the phase. The first-order harmonics at the incident wave frequencies I_1, I_2 and the second-order difference-frequency component $I^{(-)}$ are all computed in this way.

Considering the computational time of CFD simulations, the estimation of harmonic components of wave elevation and wave loads from Eq. (9) are calculated based on 10-min steady-state simulations. The estimated pitch moments in P5 from the CFD simulations at different time durations are compared in Table 6. As shown, the difference-frequency wave loads based on 300 s are within 7% of the results after 600 s.

4.2. Estimation of the QTF

The QTF values can be represented by a series of complex numbers ($a + bi$ for $\omega_1 \geq \omega_2$ and $a - bi$ for $\omega_1 \leq \omega_2$). Hence, the difference-frequency wave loads in bichromatic waves are approximated by

$$\begin{aligned} F_d(t) = & F_{12}(t) + F_{21}(t) = \text{Re}\big[A_1 A_2 \big\{(a+bi)e^{-i((\omega_1 t - \xi_1) - (\omega_2 t - \xi_2))} \\ & + (a - bi)e^{-i((\omega_2 t - \xi_2) - (\omega_1 t - \xi_1))}\big\}\big] \\ = & 2A_1 A_2\{[a\cos(\xi_1 - \xi_2) + b\sin(\xi_1 - \xi_2)]\cos(\omega_1 t - \omega_2 t) \\ & + [-a\sin(\xi_1 - \xi_2) + b\cos(\xi_1 - \xi_2)]\sin(\omega_1 t - \omega_2 t)\} \end{aligned}$$

(10)

where $A_1, A_2, \omega_1, \omega_2, \xi_1, \xi_2$ are the two incident wave amplitudes, frequencies and phases which can be calculated by Eq. (9). Given the cosine (F_d^c) and sine (F_d^s) parts of second-order difference-frequency wave loads from Eq. (9), the real (a) and imaginary (b) parts of the QTF can be found by solving Eq. (11).

$$\begin{cases} 2A_1 A_2[a\cos(\xi_1 - \xi_2) + b\sin(\xi_1 - \xi_2)] = F_d^c \\ 2A_1 A_2[-a\sin(\xi_1 - \xi_2) + b\cos(\xi_1 - \xi_2)] = F_d^s \end{cases} \qquad (11)$$
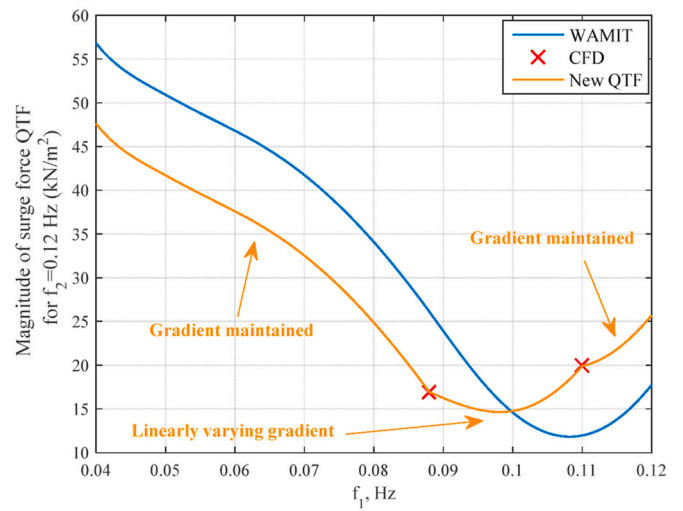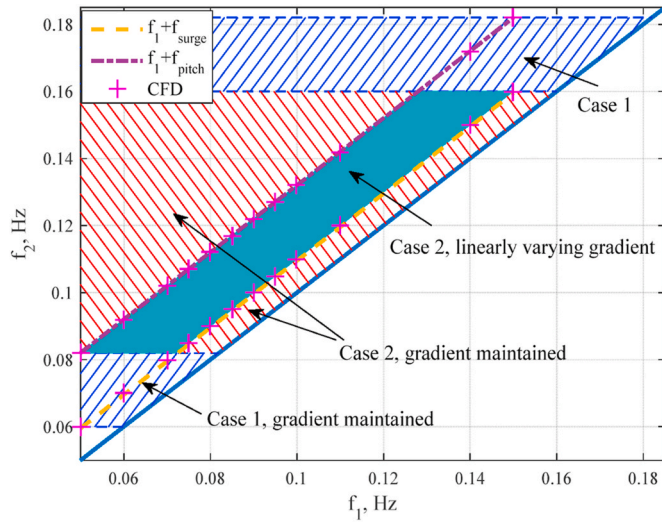
Fig. 3. Different regions of QTF for modification.

4.3. Modifying the QTFs in the SIMA models based on the CFD results

Using symmetry relations, only the upper-left-half ($f_2 \geq f_1$ in the left subplot of Fig. 3) is considered when modifying the potential flow QTFs. First, based on the CFD simulations, the surge force QTF and pitch

Fig. 4. Wave simulations, Wave S7 (Top: Time series of wave elevation in the CFD and Linear model, Bottom: Wave spectra).

Table 6
Comparisons of the estimated pitch moment at different time durations in the CFD simulations of P5.

Time (s)	1–100	1–200	1–300	1–400	1–500	1–600
0.08 Hz (MNm)	91.49	91.25	91.26	91.07	90.81	90.37
0.112 Hz (MNm)	110.7	112.5	113.4	114.1	114.5	114.4
0.032 Hz (MNm)	6.158	6.058	5.999	5.841	5.713	5.648

moment QTF along the surge and pitch natural frequencies (dashed line and dashed-dotted line in the left subplot of Fig. 3) are obtained through the method presented in Sec. 4.2. Next, the magnitudes and phases of these QTFs and the QTFs estimated by potential flow theory (WAMIT) are separately interpolated to obtain values at denser sets of frequencies (using an interval of 0.001 Hz).

Then, the interpolated results from WAMIT along the surge and pitch natural frequencies are replaced with the interpolated results from CFD simulations. To propagate the correction to other parts of the QTF, the WAMIT magnitudes or phases with the same f_2 are extracted and corrected based on the results from CFD model. There are two different cases: (1) regions with only one value from CFD model ($f_2 < 0.082$ Hz or $f_2 > 0.16$ Hz), (2) regions with two values from CFD model (0.082 Hz $\leq f_2 \leq 0.16$ Hz). In case (1), the gradient is maintained to be the same before and after modification. In case (2), the gradient is maintained outside of the surge and pitch natural frequencies ($f_1 < f_2 - 0.032$ Hz or $f_1 > f_2 - 0.01$ Hz) while the gradient varies linearly between surge and pitch natural frequencies ($f_2 - 0.032$ Hz $\leq f_1 - 0.01$ Hz). An example is shown in the right subplot of Fig. 3. Finally, this modified QTF matrix is downsampled to an interval of 0.05 Hz and implemented in the SIMA model.

5. Results

5.1. Wave loads on the upright and trimmed semi-submersible FWT in bichromatic waves

First, we examine the details of difference-frequency wave loads on a restrained semi-submersible FWT in two bichromatic waves (wave index: S7, P5). The surge forces at the wave and surge natural frequencies in wave S7 are presented in Sec. 5.1.1 and the pitch moments at the wave and pitch natural frequencies in wave P5 are shown in Sec. 5.1.2. Considering the existence of mean pitch angle for wind turbine during operation, wave loads on a 5° trimmed floater are also included. The floater is rotated 5° clockwise around Point A shown in Fig. 2. The surge force (along x axis) and pitch moment (around y axis) are
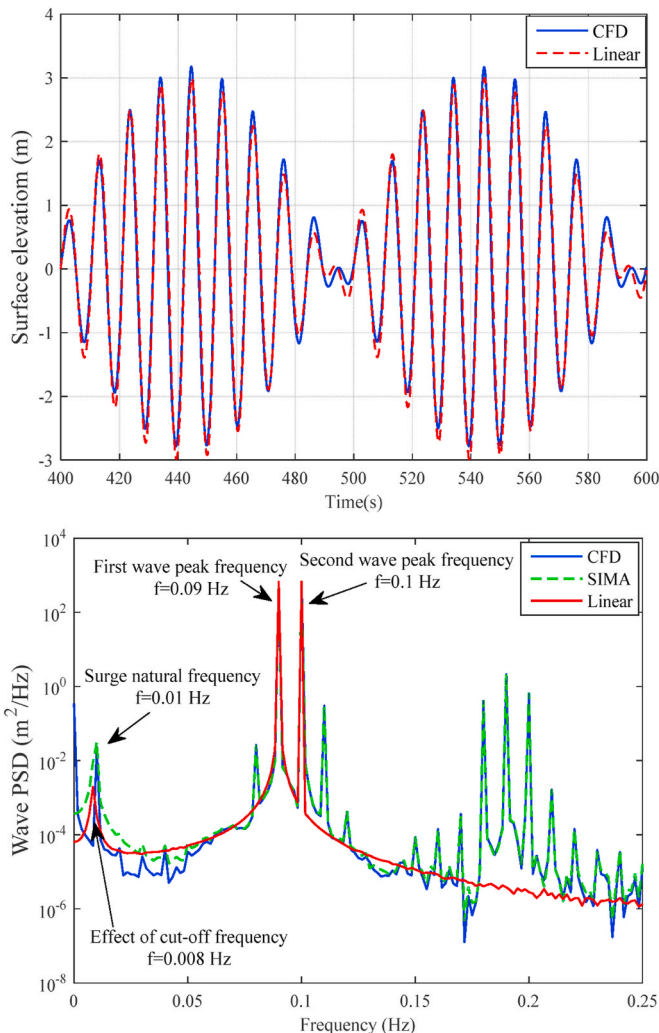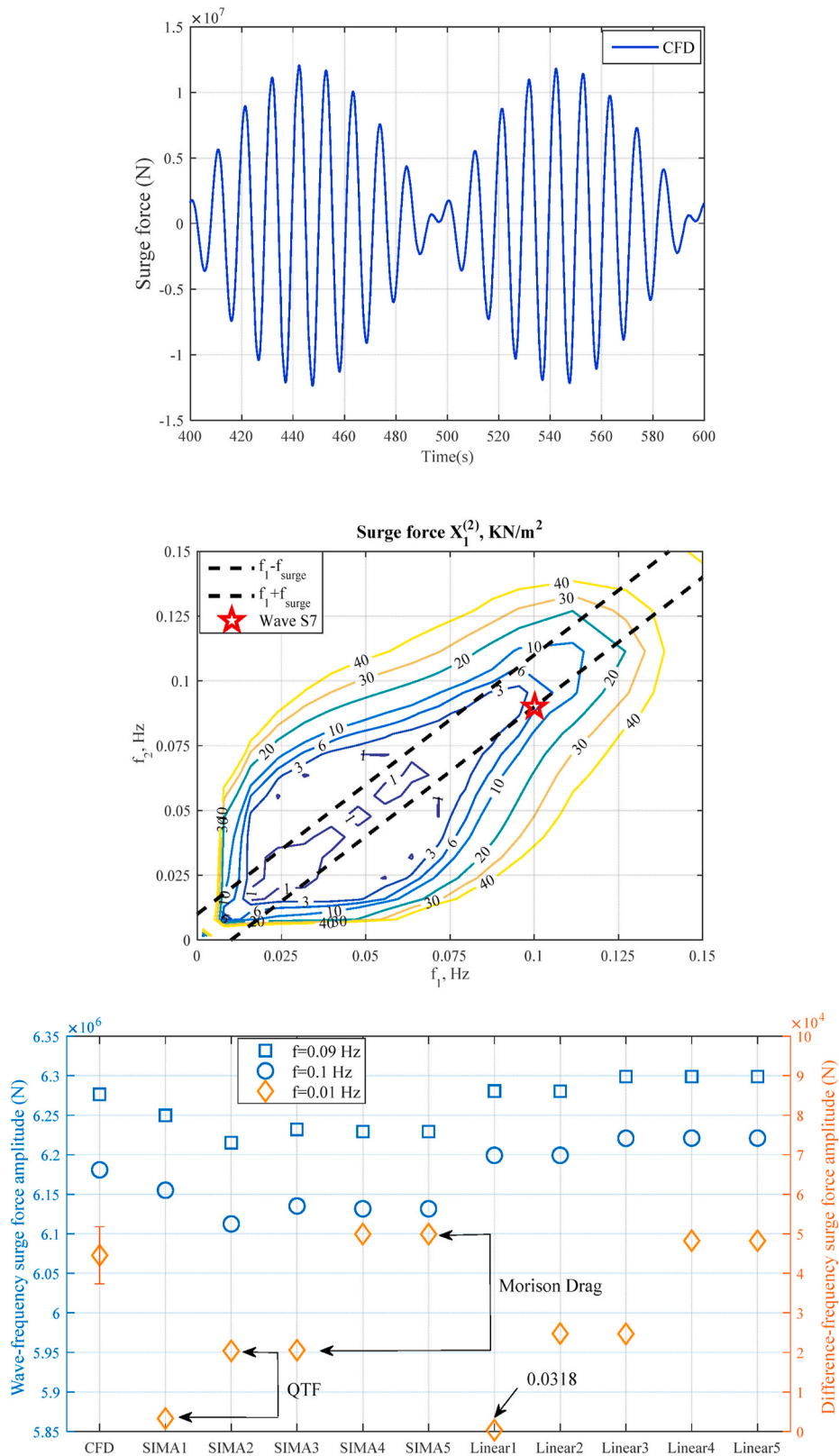
Fig. 5. Surge forces on the upright floater, Wave S7 (Top: time series of total surge forces in CFD simulations, Middle: QTF used in SIMA simulations, Bottom: Surge forces at the wave frequencies and surge natural frequency. The uncertainty bar represents the numerical uncertainty of difference-frequency surge force, the uncertainty in the wave-frequency surge force from CFD is given in Table 4).
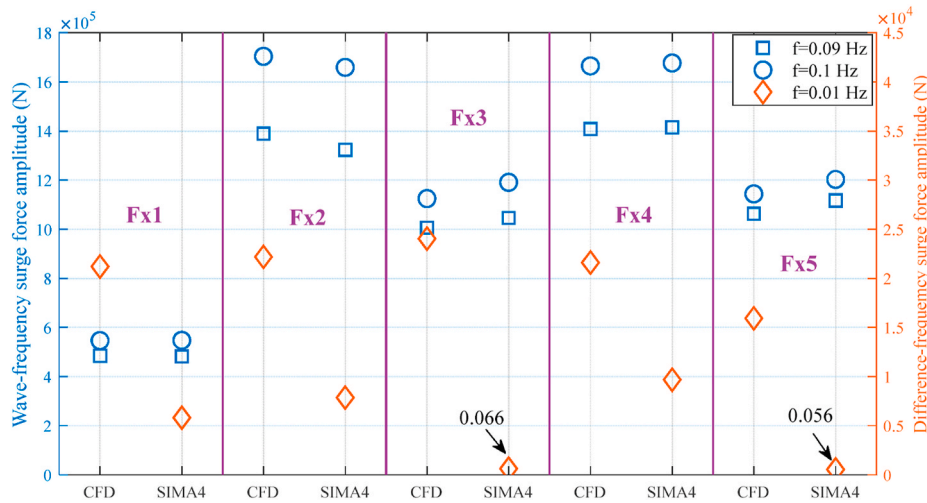
Fig. 6. Surge forces on the separated columns of upright floater, Wave S7 (Fx1: main column, Fx2: upper part of upstream column, Fx3: lower part of upstream column, Fx4: upper part of starboard column, Fx5: lower part of starboard column. See Fig. 2 for the definitions of columns).
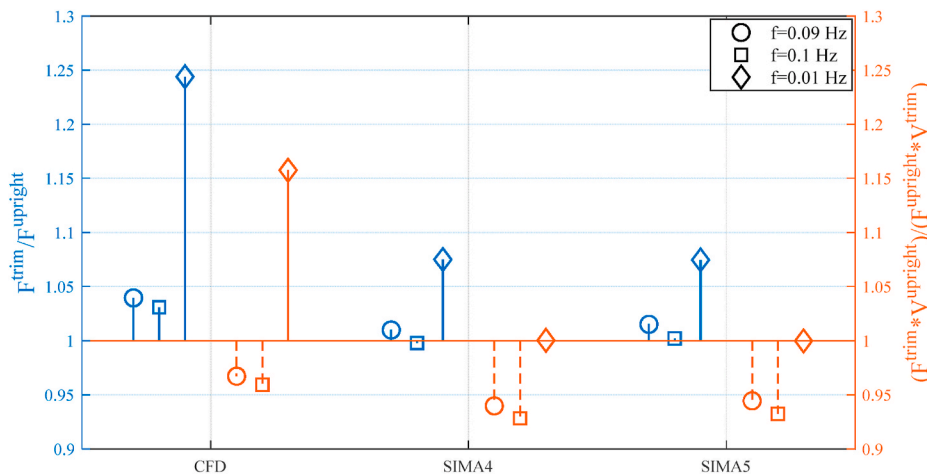
Fig. 7. Comparisons of surge forces on the upright and trimmed floaters, Wave S7.

calculated in the same global coordinate system as the upright condition (Fig. 2).

5.1.1. Bichromatic wave S7

The wave elevation for wave S7 in the CFD and SIMA models is shown in Fig. 4. No significant wave damping can be observed at the end of the CFD simulations. A comparison of CFD and 'Linear' shows the interaction between two regular waves which leads to the peaks between 0.15 Hz and 0.25 Hz, at frequencies such as $f_1 + f_2$, or $2f_1$, or $2f_2$. The wave amplitudes at these sum frequencies are much smaller than the wave-frequency amplitudes (note the log scale in the PSD). The wave amplitudes at the wave frequencies agree with the analytical solution (1.5 m) within 1%. At the difference frequency (the surge natural frequency), the wave amplitude from the CFD model is 9.9% smaller than the second order analytical solution (0.0101 m). As expected, the wave amplitude of the first-order bichromatic wave (Linear) at the surge natural frequency is negligible (0.001 m). The effect of the cut-off frequency (0.008 Hz) is, however, visible in the PSD of the 'Linear' wave elevation.

The total surge force on the upright floater from the CFD simulation is presented together with SIMA simulations in Fig. 5. There is a small numerical damping of the surge force caused by the large turbulent viscosity at the floater boundaries in the CFD simulation.

Compared to the CFD simulations, SIMA slightly underpredicts the surge forces at the wave frequencies (within 1.2%, smaller than the uncertainty of CFD results). In the SIMA models, the linear wave force transfer function dominates at the wave frequencies. The surge forces at the surge natural frequency are mainly from the QTF (SIMA2) and the integration of the Morison drag forces to the linear free surface (SIMA4). SIMA4 overpredicts the surge force at the surge natural frequency by 11% compared to the CFD estimations. The axial drag forces on the heave plates have no effect on the surge forces (SIMA4 vs SIMA5). The surge forces using the first-order bichromatic wave (Linear) are also shown in Fig. 5. A comparison of 'SIMA1' vs 'SIMA2' and 'Linear1' vs 'Linear2', shows that the force contributions from the QTF reduce the surge forces at the wave frequencies if the difference frequency between wave components at other frequencies (Fig. 4) coincides with wave frequencies. Furthermore, the contribution of difference-frequency wave components via the linear wave force transfer function (SIMA1 vs Linear1) decreases the difference-frequency surge force (SIMA2 vs Linear2). In addition, 'Linear' models give the same conclusions as 'SIMA' models.

Fig. 6 compares the surge forces on individual columns of the upright floater between SIMA and CFD simulations. In these cases, the QTF for each column is not included in SIMA results. For each column, the surge forces at the second wave frequency (0.1 Hz) are larger than the forces at
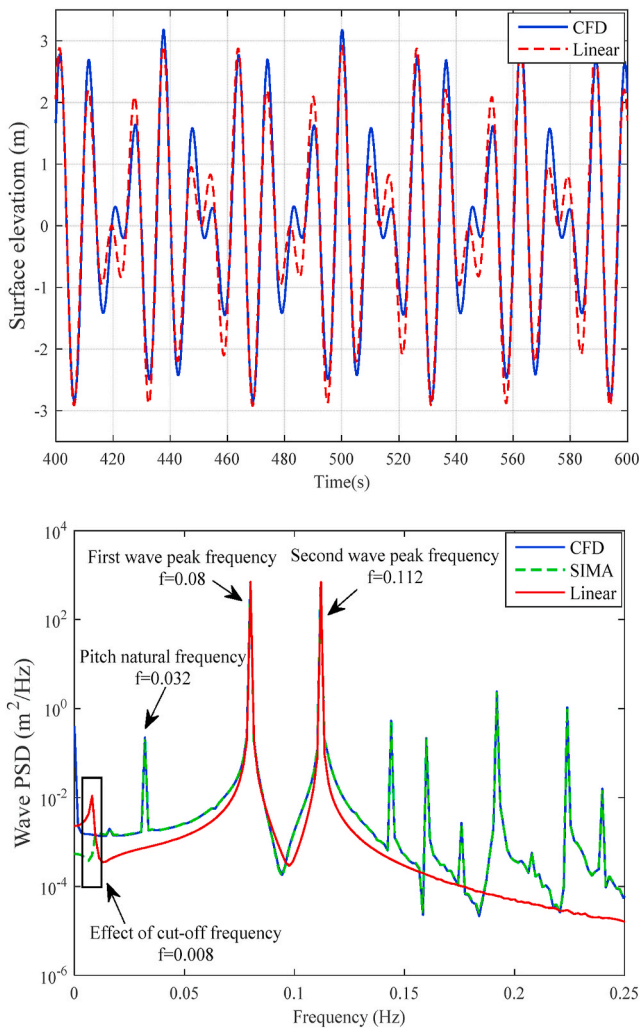
Fig. 8. Wave simulations, Wave P5 (Top: Time series of wave elevation in the CFD model, Bottom: Wave spectra).

the first wave frequency (0.09 Hz), which is opposite the results for total surge forces (Fig. 5). This is due to the frequency-dependent phase differences of surge forces on each column. In addition, all the numerical models predict similar results for the surge forces at the wave frequencies. No matter for the upstream column or the starboard column, although the diameter of lower part is twice than that of upper part, the surge force on the upper part (Fx2 and Fx4) is larger compared to the force on the lower part (Fx3 and Fx5) at the wave frequencies. That is because the wave acceleration decreases as one moves further downward. The surge forces at the wave frequencies on the starboard column (Fx4 and Fx5) are not significantly different from those on the upstream column (Fx2 and Fx3).

Due to the lack of the QTF for each column, the surge forces at the difference frequency in the SIMA simulations mainly come from the integration the Morison drag force to the linear free surface. Compared to the CFD results, one can observe that SIMA underpredicts the surge forces on each column at the surge natural frequency and larger underprediction occurs at the lower part of columns (Fx3 and Fx5). In addition, in the CFD simulations, the surge forces at the surge natural frequency on the starboard column (Fx4 and Fx5) are smaller than those on the upstream column (Fx2 and Fx3) and a larger reduction (33%) is found at the lower part of columns (Fx3 vs Fx5).

The surge forces on the trimmed and upright floaters are compared in Fig. 7. For the CFD simulations, the surge forces on the trimmed floater at the wave frequencies increase by 4% compared to the upright

condition. In the SIMA4 model, the linear wave force transfer function is dominant at the wave frequencies. Hence, for the trimmed floater, the increasing or decreasing surge forces at the wave peak frequencies mainly depend on the effect of the changed immersed geometry of the floater on the first-order hydrodynamic properties. The effect of axial drag forces is shown in 'SIMA5' of Fig. 7. As expected, for the trimmed floater, the axial drag forces on the heave plates have a component along the x axis which slightly increases the surge force. To eliminate the effect of changed submerged volume, comparisons between surge force amplitudes normalized by the mean displaced submerged volume V are shown in the right y axis of Fig. 7. A larger portion of the columns is under water after rotating the floater. Meanwhile, the water particle acceleration at the same position on the columns decreases for the trimmed floater. Considering the changed volume, the surge forces at the wave frequencies under trimmed condition decrease in all the numerical simulations.

An increased surge force at the surge natural frequency is seen for the trimmed condition. Compared to the CFD simulations, the increases in the SIMA models are small. In the SIMA simulations, the axial drag forces on the heave plates have minor contributions to the surge force on the trimmed floater at the surge natural frequency (SIMA4 vs SIMA5), considering small trimmed angle. The difference-frequency force in CFD increases more than the change in volume, but this is not the case in the SIMA models. For a trimmed floater, the flow separation around the edge of heave plate is more significant and the Morison drag force underestimates this effect. This big difference also highlights that the accuracy of estimated difference-frequency wave loads in the engineering tools is sensitive to the drag coefficients. Even a small change can result in a large variation for the drag coefficients.

5.1.2. Bichromatic wave P5

The wave simulations of Wave P5 are compared in Fig. 8. Like Wave S7, no significant wave damping can be seen at the end of the CFD simulations and interaction between two regular waves is also observed (CFD vs Linear). There is good agreement (within 1.67%) between the analytical solution and different numerical models at the wave frequencies. The wave amplitude at the pitch natural frequency in the CFD model is 4.2% larger than the analytical solution of 0.0257 m.

The pitch moments on the upright floater estimated by the CFD model are compared with SIMA models in Fig. 9. Like the surge force, at the end of the CFD simulations, the pitch moment slightly attenuates with time due to the increased turbulent viscosity at the boundaries of the floater.

Compared to the CFD simulations, all the SIMA models predict similar pitch moments at the wave frequencies (within 2.6%, smaller than the uncertainty of CFD results) and pitch natural frequency (within 3.6%) except for a large underprediction of pitch moment at the pitch natural frequency using SIMA1 model. Both in the 'SIMA' and 'Linear' models, the linear wave force transfer function is dominant at the wave frequencies. Meanwhile, the axial drag forces on the heave plates (SIMA5 and Linear5) increase the pitch moments at the wave frequencies. The pitch moment from the QTF (SIMA2 and Linear2) dominates at the pitch natural frequency. The effect of difference-frequency wave components on the difference-frequency pitch moment is minor (SIMA2 vs Linear2). Other force contributions have minor influence at the pitch natural frequency.

The numerically estimated pitch moments on the upright and trimmed floater are compared in Fig. 10. For the CFD simulations, the pitch moment on the trimmed floater increases by about 11% at the first wave frequency (0.08 Hz), but decreases slightly (0.15%) at the second wave frequency (0.112 Hz) compared to the moments on the upright floater. In the SIMA4 simulations, for the trimmed floater, an increasing moment (8.8%) occurs at the first wave frequency and a reduction of moment (4.5%) appears at the second wave frequency. All the variations at the wave frequencies are due to the changed frequency-dependent hydrodynamic properties of the floater. Combining the exact values in Fig. 9
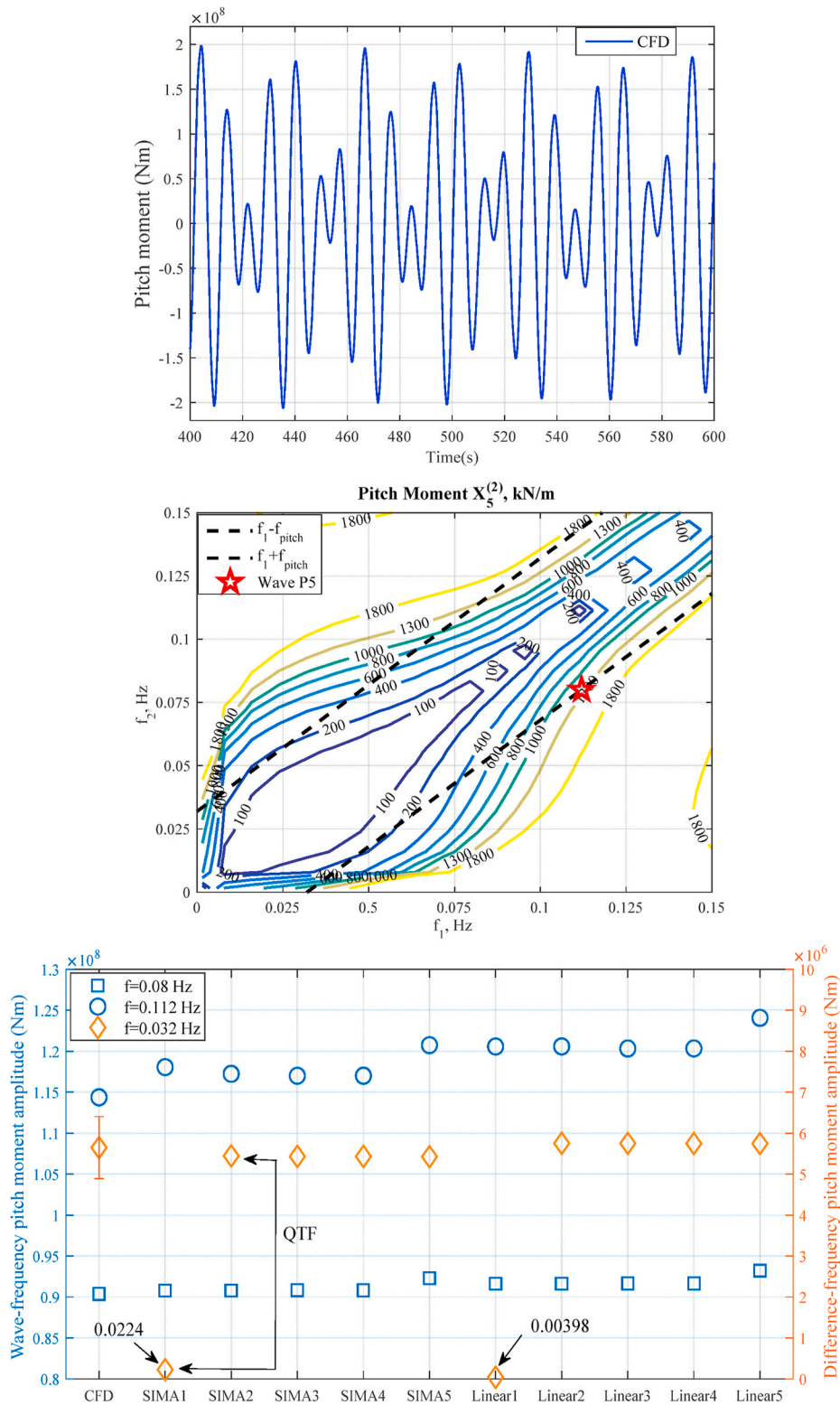
Fig. 9. Pitch moments on the upright floater, Wave P5 (Top: Time series of total pitch moments in CFD simulations, Middle: QTF used in SIMA simulations, Bottom: Pitch moments at the wave frequencies and pitch natural frequency. The uncertainty bar represents the numerical uncertainty of difference-frequency pitch moment, the uncertainty for the wave-frequency pitch moment from CFD can be found in Table 4.).

and ratios in Fig. 10, pitch moments on the trimmed floaters slightly increase both at the first and second wave frequency compared to the upright floater when considering the axial drag forces on the heave plate (SIMA5). Like the surge forces, the effect of changed volume is removed in the comparison of pitch moments shown in the right *y* axis of Fig. 10.

Consideration of changed volume leads to a decreasing pitch moment at the second wave frequency under trimmed condition and has minor influence at the first wave frequency in all the numerical simulations.

The pitch moment on the trimmed floater at the pitch natural frequency increases by 1.7% for the CFD model compared to the one under
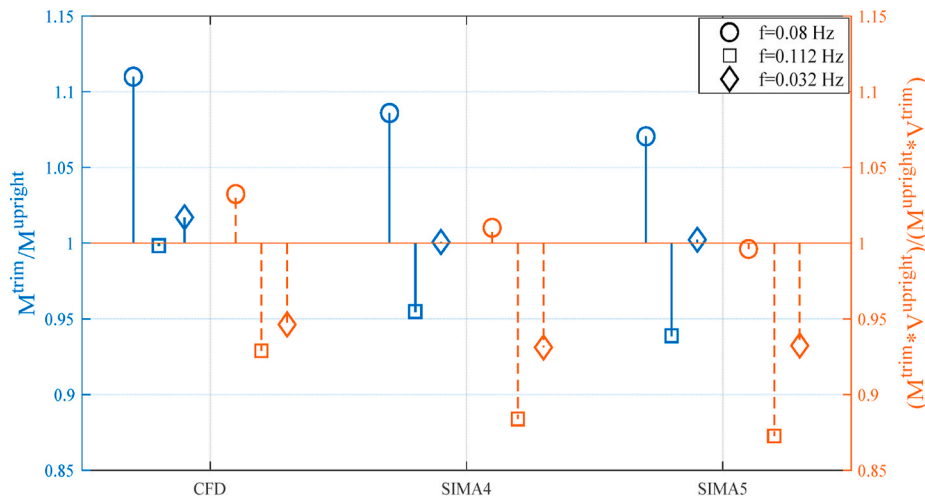
Fig. 10. Comparisons of the pitch moment on the upright and trimmed floaters, Wave P5.

Table 7
Pitch moment amplitudes at the pitch natural frequency, SIMA 2, Wave P5.

	Pitch Moment amplitude (Nm)
Upright position	5.4433E6
Trimmed position	5.4183E6

upright condition. In SIMA models, the effect of 5° mean pitch angle on the pitch moment at the pitch natural frequency is not significant. This is mainly caused by the small change in the contribution from the QTF, which is shown in Table 7. Like the upright condition, the axial drag forces on the heave plates (SIMA5) have minor contributions at the pitch natural frequency. Furthermore, the increase in the pitch moment at the pitch natural frequency is smaller than the increase in the submerged volume.

5.2. Comparisons and modifications of QTFs in bichromatic waves

As shown in Table 1, 24 sets of bichromatic waves were selected to calculate the QTFs of a restrained upright semi-submersible FWT and modify the QTFs from potential flow theory. The QTFs before modification are presented in Sec. 5.2.1, while modifications are presented in Sec. 5.2.2, and the validations in an irregular wave are shown in Sec. 5.3.

5.2.1. Initial QTF comparisons

Using the approach from Sec. 4.2, the magnitudes of surge force and pitch moment QTFs are calculated based on different numerical models and presented in Fig. 11. CFD and SIMA5 model agree well at the lower wave frequencies, while the CFD model predicts larger difference-frequency wave loads at higher wave frequencies. The contributions of the difference-frequency wave by linear wave force transfer function (SIMA1) are negligible in the low-frequency range except for the surge forces at the pitch natural frequency. For the surge forces at the surge natural frequency, the contributions of Morison drag forces (differences between SIMA2 and SIMA5) decrease with increasing wave frequencies, while the influences of Morison drag forces on the surge forces at the pitch natural frequency are not significant. In addition, the pitch moments from the QTFs (SIMA2 vs SIMA5) dominate in the low-frequency range in the SIMA model.

5.2.2. QTF modification

Prior to following the modification procedure from Sec. 4.3, several effects must be treated specially. In the SIMA model, viscous effects are

considered by a Morison-type load model. Furthermore, the difference-frequency wave components (from treating the CFD-generated wave elevation as linear) also contribute to the difference-frequency wave loads through the linear wave force transfer function. Hence, these two effects are removed from the QTFs estimated from CFD simulations. The CFD results after subtracting these effects are referred to as 'New QTF'. 'Old QTF' is the QTFs estimated in WAMIT. Assuming that the Morison model captures the viscous effects up to third order and that even higher order effects are small, the 'New QTFs' are directly applied in the validation against the irregular wave (Section 5.3) even though the wave height in the bichromatic wave conditions (Table 1) differs from the wave height in the irregular-wave spectrum (7.1 m).

The magnitudes and phases of surge force and pitch moment QTFs estimated based on the CFD results are compared with the potential flow theory calculations in Fig. 12. At the lower wave frequencies (generally <0.1 Hz), there is little discrepancy between CFD and potential flow theory in predicting the magnitudes of surge force and pitch moment QTFs. However, a larger difference is observed at higher wave frequencies (generally >0.1 Hz) with the CFD model giving larger magnitudes. For the phase of surge force and pitch moment QTFs, the CFD model gives approximately the opposite phase compared to the potential flow theory, which illustrates the limitation of the engineering tools in accurately estimating the phase of difference-frequency wave loads. This large discrepancy cannot be captured by tuning the Morison drag term, which simply changes the results 90° out of phase.

The magnitudes and phases of modified surge force QTFs in the low-frequency range are presented together with the QTFs from potential flow theory in Fig. 13. Close to the surge natural frequency, the new QTFs have smaller magnitudes for lower incident wave frequencies (0.05–0.09 Hz). For higher incident wave frequencies, the new QTFs have higher magnitudes. Furthermore, for low incident wave frequencies, the phase is approximately opposite compared to the phase of QTFs from potential flow theory.

The comparisons of pitch moment QTFs in the low-frequency range are presented in Fig. 14. Compared to the QTFs from potential flow theory, the modified QTFs have similar shape and magnitude except for the larger values at the higher wave frequencies. Like the surge force QTFs, the modified pitch moment QTFs have almost opposite phases compared to the QTFs from potential flow theory. Furthermore, the modified QTFs have a bigger gradient in the phase around the mean drift moment diagonal. The phase of QTFs from potential flow theory has a local peak/trough around the pitch natural frequency. However, this local peak/trough is transferred to the regions between surge and pitch natural frequencies in the modified QTFs due to the approach applied in the QTF modification.
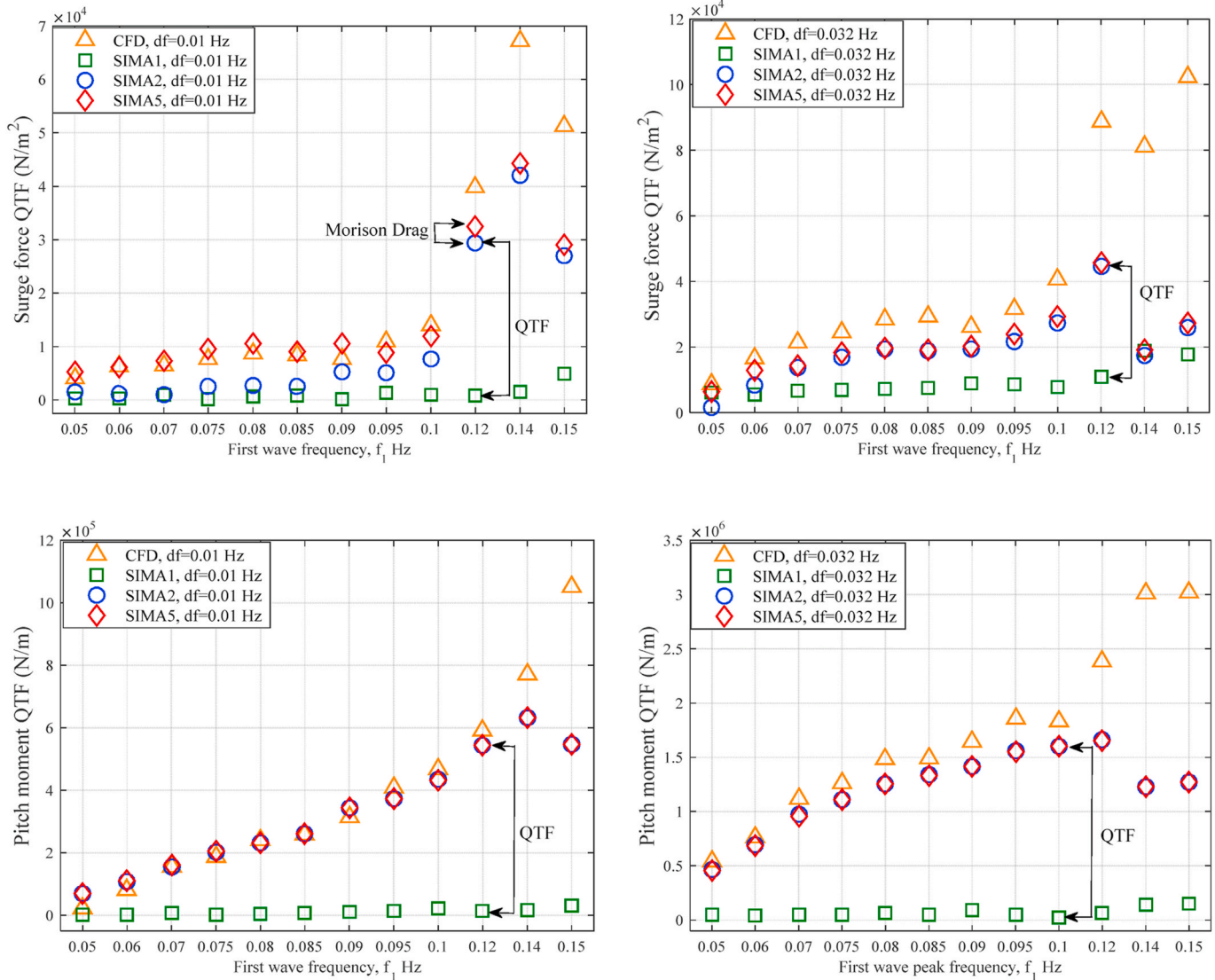
Fig. 11. The magnitudes of surge force and pitch moment QTFs at different wave frequencies (Top: Surge force QTF at the surge (left) or pitch (right) natural frequency, Bottom: Pitch moment QTF at the surge (left) or pitch (right) natural frequency).

To check the implementation of the QTF modification, the difference-frequency wave loads predicted by the SIMA model with modified QTFs (SIMA6) in bichromatic waves are compared against the CFD results in Fig. 15. The difference-frequency wave loads estimated by the SIMA model with modified QTFs (SIMA6) are, as expected, close to the CFD results. There is a better agreement among different numerical models at the surge natural frequency compared to the results at the pitch natural frequency. In the current study, the bichromatic waves are chosen such that the difference corresponds to the surge or pitch natural frequency. Hence, there is a lack of CFD results in the upper-left and lower-right corners of QTF matrix (Fig. 3), which leads to a slightly larger difference at the pitch natural frequency. The largest difference occurs when estimating the wave loads at the pitch natural frequency with the maximum first wave frequency (0.15 Hz). Here, the second wave frequency is 0.182 Hz, close to the maximum frequency (0.185 Hz) in the QTFs from WAMIT. The uncorrected data between 0.182 Hz and 0.185 Hz can explain the difference. Overall, around the peak frequencies of the irregular wave in Sec. 5.3 (0.083 Hz), the numerically estimated difference-frequency wave loads by SIMA model with modified QTFs agree well with CFD results.

5.3. Validation of modified QTFs against experimental data

In this part, the experimentally measured wave elevation at the origin is input into SIMA software by a high-pass filter with a 0.008 Hz cut-off frequency. In order to assess the capability of modified QTFs in estimating the difference-frequency wave loads, a response metric (referred to 'PSD sum') is adopted in the current study based on work from Robertson et al., (2020). The 'PSD sum' is an integration of the force or moment spectrum in the low-frequency range. The frequency limits for the integration are 0.005–0.05 Hz.

The numerically estimated difference-frequency surge forces in SIMA model with modified QTFs (SIMA6) and QTFs from WAMIT (SIMA5) are compared against experimental measurements in Fig. 16. Compared to the results with QTFs from WAMIT, the difference-frequency surge force estimated by the modified QTFs agrees better with the experiment data. However, around the surge natural frequency, the modified QTFs still underpredict the wave loads. As shown in the right subplot of Fig. 16, the difference-frequency surge force PSD sums are calculated for both experimental and numerical results. The improvement using the modified QTFs is significant. The underestimation of the PSD sum is reduced to 2.34% for modified QTFs from 55.07% for the QTFs from WAMIT. This validation also indicates that the CFD model can give better
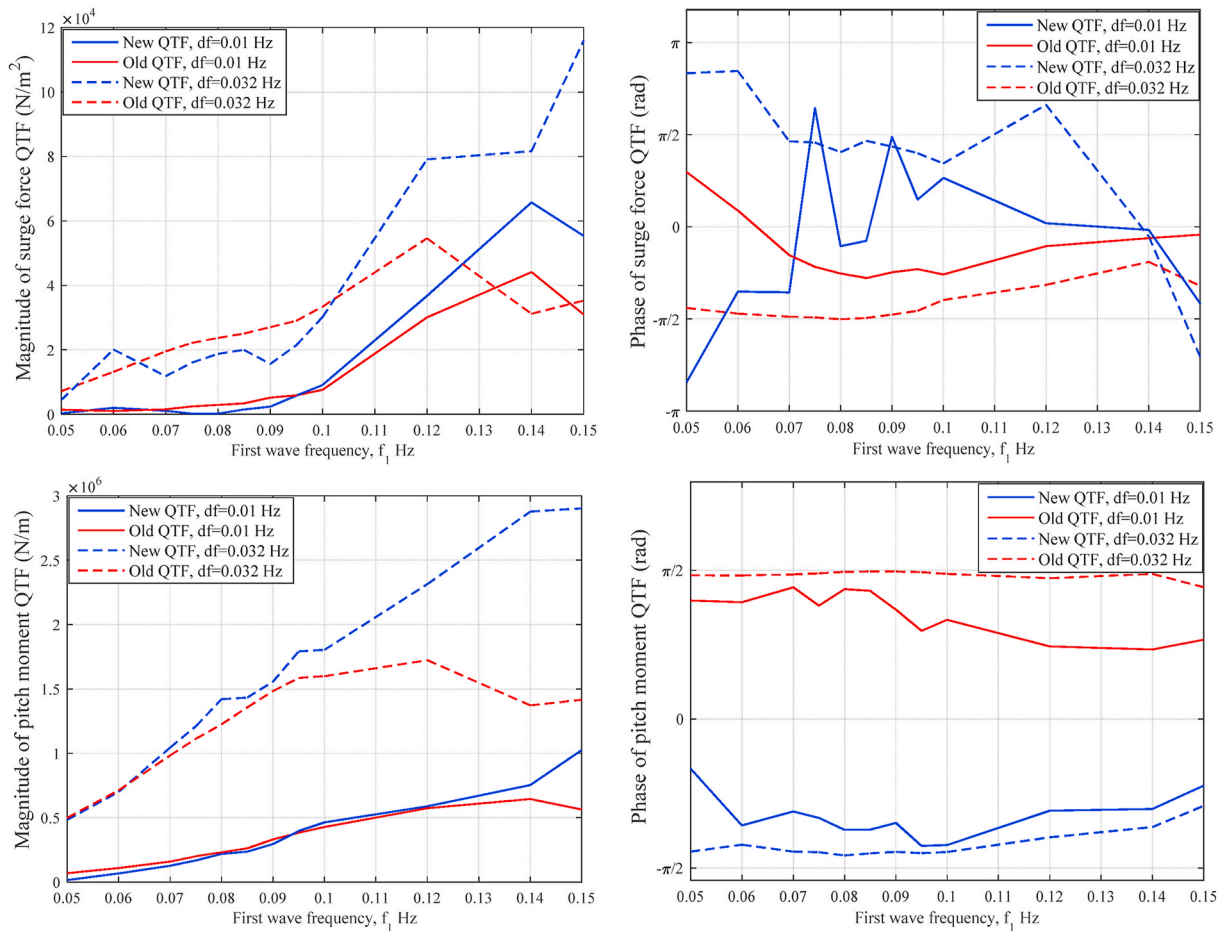
Fig. 12. The magnitudes and phases of the calculated QTFs at the surge and pitch natural frequency based on CFD simulations and potential flow theory.

estimation of difference-frequency surge forces, but has limitations in capturing the surge forces at even lower frequencies.

The numerically estimated difference-frequency pitch moments are compared against experimental measurements in Fig. 17. Like the modified surge force QTFs, there is a better agreement of difference-frequency pitch moment between experiment and SIMA model with the modified QTFs (SIMA6). Compared to the experimental results, the difference-frequency pitch moment PSD sum with modified QTFs is 11.91% smaller while the result with the QTFs from WAMIT is 42.71% smaller.

Overall, one can conclude that the SIMA with modified QTFs (SIMA6) can better capture difference-frequency wave loads than the QTFs from potential flow theory. This also demonstrates the advantages of the CFD model in capturing the nonlinear difference-frequency wave loads. The more CFD simulations at different sets of frequencies are carried out, the more accurate the modified QTFs are, and the better the difference-frequency wave loads are captured by SIMA models with modified QTFs.

5. Conclusions

In the current work, two numerical models are used to study the nonlinear difference-frequency wave loads on a restrained semi-submersible FWT in bichromatic waves: a CFD model and a potential flow theory model with Morison-type drag (SIMA). Furthermore, the results from CFD model are used to modify the QTFs from potential flow theory, and the resulting model is validated against experimental data in an irregular wave.

The wave loads from CFD and the potential flow model are in good

agreement at the wave frequencies. In the SIMA model, the difference-frequency surge force at the surge natural frequency is mainly from the integration of Morison drag force to the linear free surface. This contribution decreases with increasing wave frequencies, and the surge force from QTFs becomes dominant. At the pitch natural frequency, the pitch moment from QTFs is dominant. In addition, the axial drag forces on the heave plates only increase the pitch moment at the wave frequencies and have minor contributions to the difference-frequency wave loads.

In order to better understand the effects of the multimember arrangement of the semi-submersible floater, surge forces on each column are extracted. Compared to the CFD results, SIMA underpredicts the difference-frequency surge forces on each column and a larger underprediction is seen at the lower part of the columns. In addition, in the CFD simulations, the surge forces at the surge natural frequency on the starboard column are smaller than those on the upstream column and a larger reduction is found at the lower part of columns.

The effects of 5° mean pitch angle during wind turbine operation on the difference-frequency wave loads are also investigated. The wave loads are calculated based on the global coordinate system used in up-right condition. The variations at the wave frequencies are mostly due to the changed immersed geometry and correspondingly changed first-order hydrodynamic properties of the floater. At the surge natural frequency, there is an increase in surge force in both CFD and the potential flow model, but the increase in the CFD model is more significant. The pitch moments under the trimmed condition are not significantly changed compared to the upright floater. However, the effects of trim on the motions and loads in the mooring system of FWTs are of still interest in the future research.
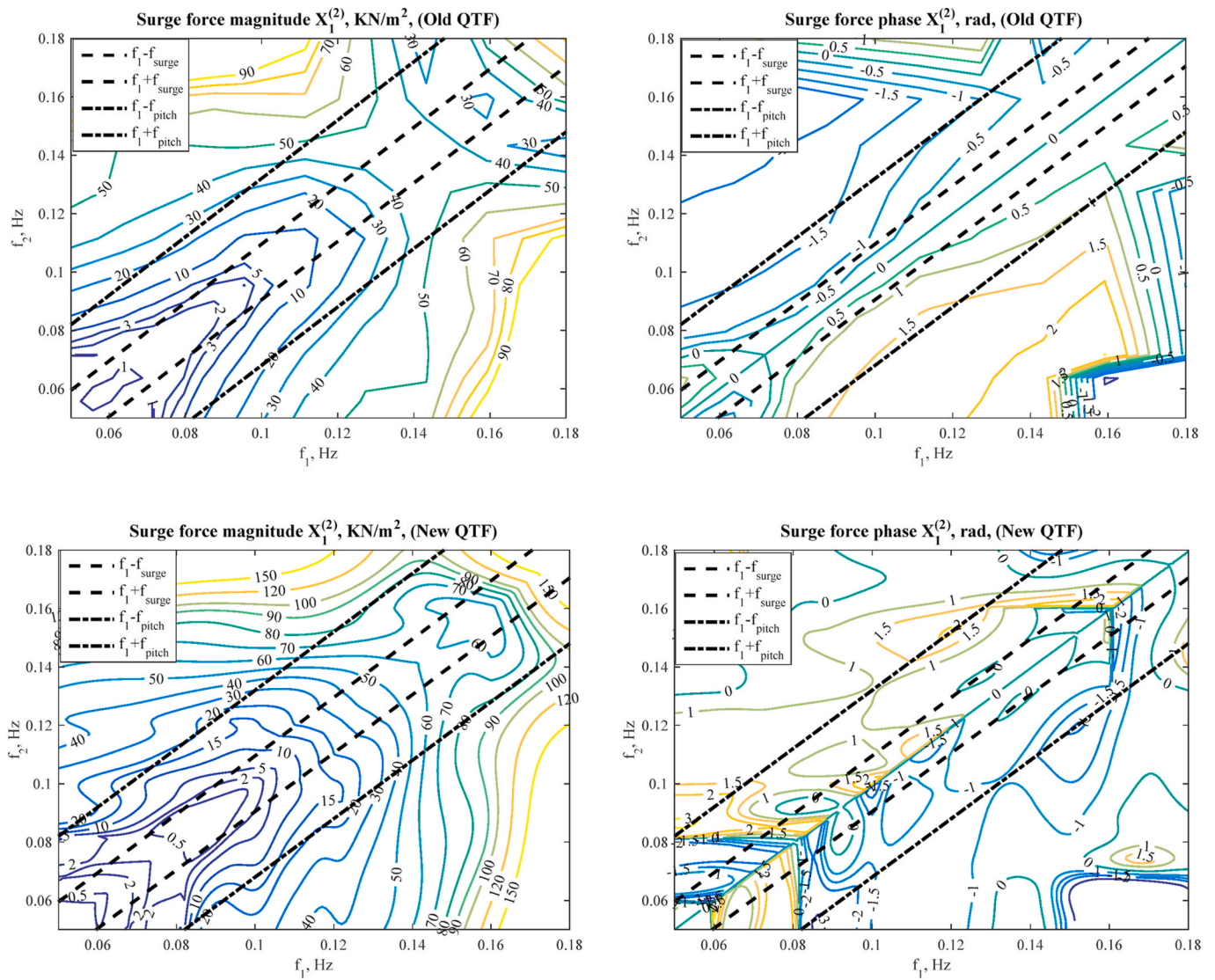
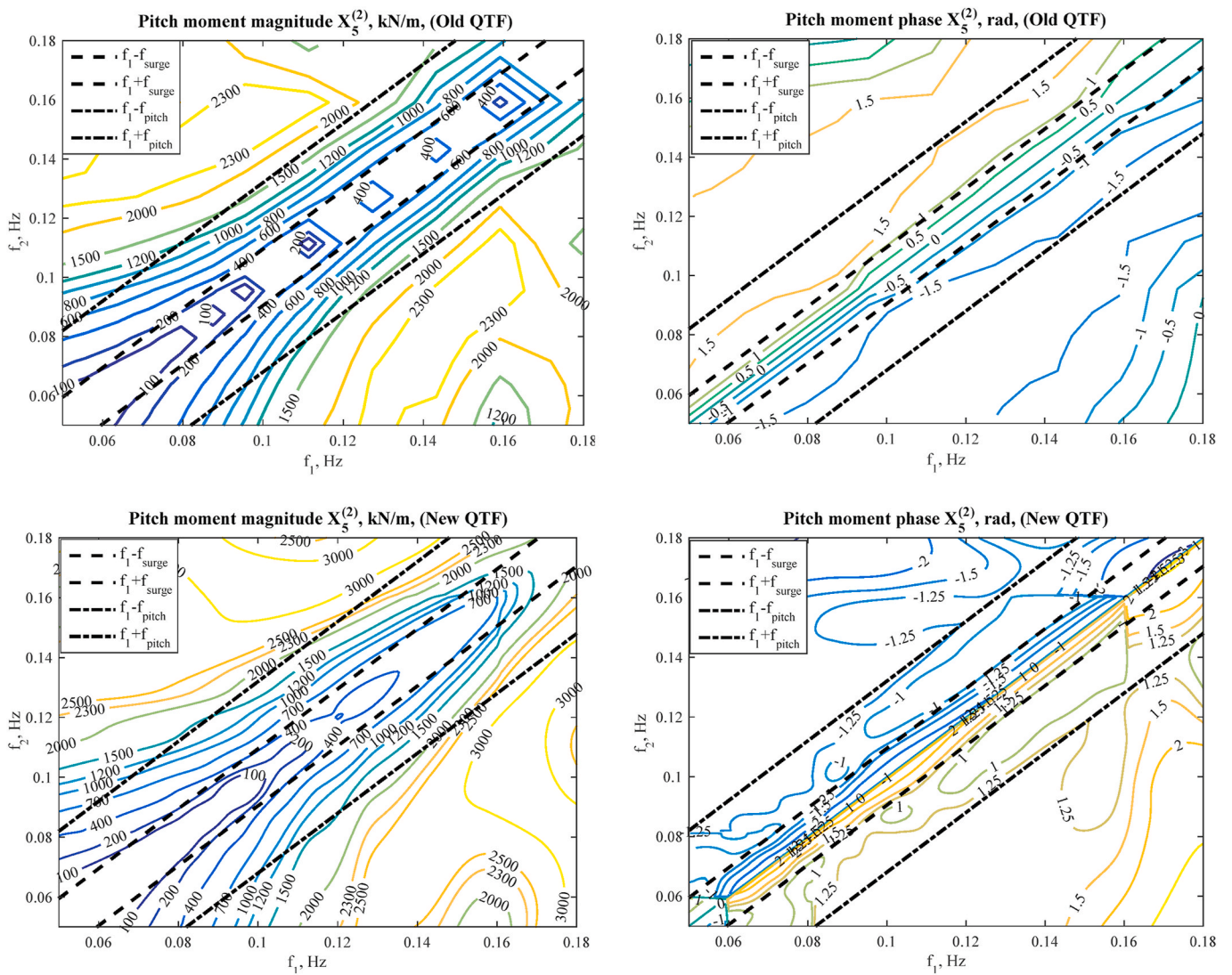**Fig. 13.** Magnitudes and phases of surge force QTFs in the low-frequency range.

Fig. 14. Magnitudes and phases of pitch moment QTFs in the low-frequency range.

When modifying the QTFs based on CFD simulations, larger modifications in the magnitude are seen to be required at higher wave frequencies. Interestingly, the CFD model gives approximately the opposite

phase compared to the original potential flow results. The modification of the QTFs is verified by checking that difference-frequency wave loads estimated by the SIMA model with modified QTFs are close to the CFD
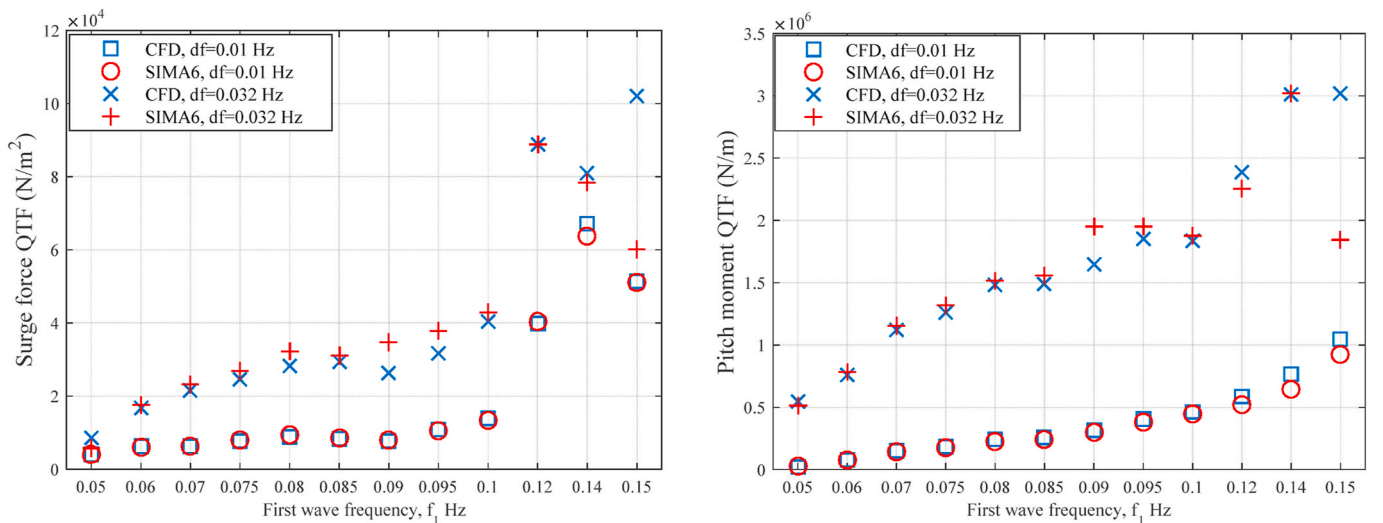
Fig. 15. Difference-frequency wave loads estimated in CFD model and SIMA model with modified QTFs.
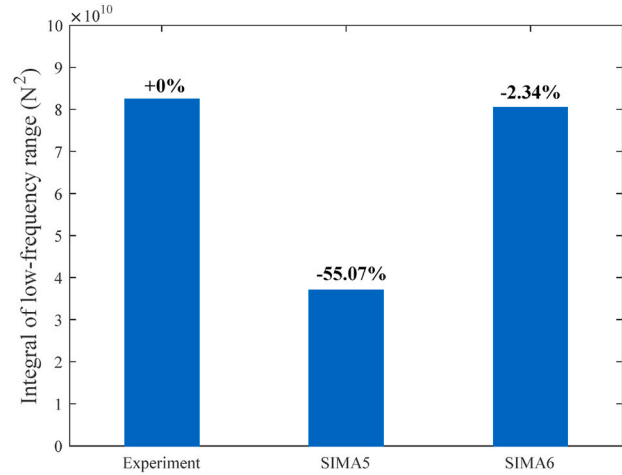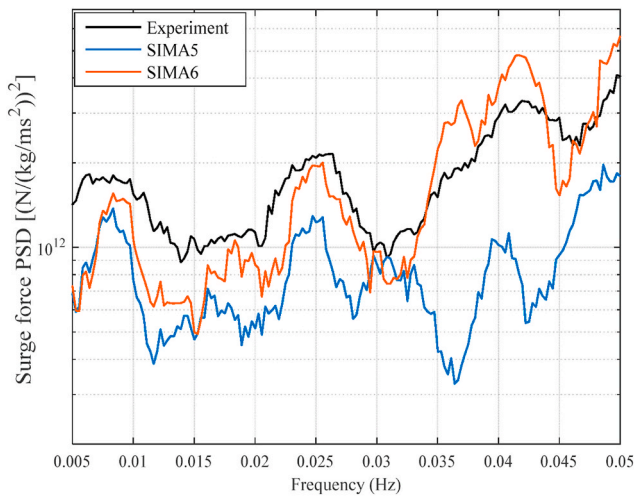
Fig. 16. Difference-frequency surge force in an irregular wave (left: surge force spectra in low-frequency range, right: difference-frequency surge force PSD sum metric).
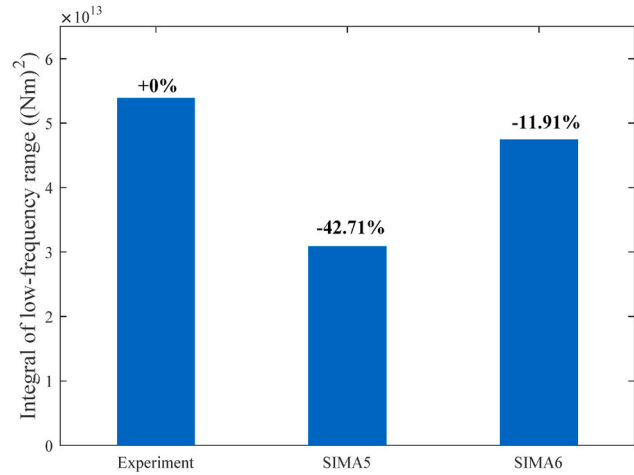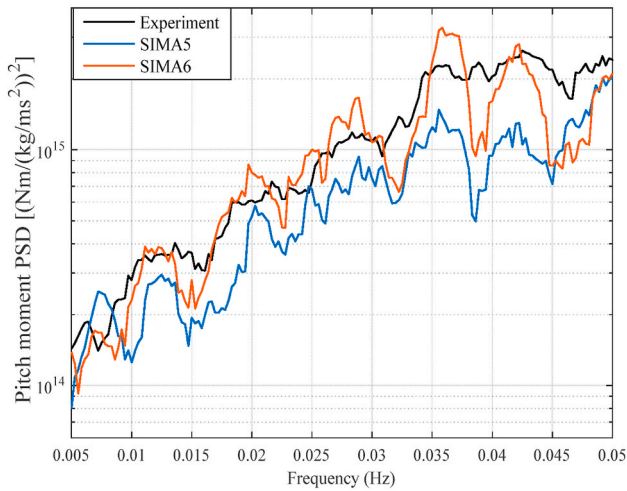

Fig. 17. Difference-frequency pitch moment in an irregular wave (left: pitch moment spectra in low-frequency range, right: difference-frequency pitch moment PSD sum metric).

results in bichromatic waves. The approach is then compared to experimental measurements of difference-frequency wave loads in an irregular wave. The modified QTFs significantly reduce under-prediction of difference-frequency wave loads compared to the QTFs from potential flow theory.

CRediT authorship contribution statement

Haoran Li: Conceptualization, Methodology, Software, Validation, Investigation, Formal analysis, Data curation, Writing – original draft. **Erin E. Bachynski-Polić:** Conceptualization, Methodology, Resources, Writing – review & editing, Supervision.

Declaration of competing interest

The authors declare that they have no known competing financial interests or personal relationships that could have appeared to influence the work reported in this paper.

References

Bachynski, E.E., Thys, M., et al., 2016. Real-time Hybrid Model Testing of a Braceless Semi-submersible Wind Turbine: Part II—Experimental Results. ASME 2016 35th International Conference on Ocean, Offshore and Arctic Engineering. American Society of Mechanical Engineers Digital Collection.

Benitz, M.A., Schmidt, D.P., et al., 2014. Comparison of Hydrodynamic Load Predictions between Reduced Order Engineering Models and Computational Fluid Dynamics for the OC4-DeepCwind Semi-submersible. No. NREL/CP-5000-61157. ASME 2014 33rd International Conference on Ocean, Offshore and Arctic Engineering. American Society of Mechanical Engineers Digital Collection.

Benitz, M.A., Schmidt, D.P., et al., 2015. Validation of Hydrodynamic Load Models Using CFD for the OC4-DeepCwind Semisubmersible. No. NREL/CP-5000-63751. ASME 2015 34th International Conference on Ocean, Offshore and Arctic Engineering. American Society of Mechanical Engineers Digital Collection.

Berberović, E., van Hinsberg, N.P., et al., 2009. Drop impact onto a liquid layer of finite thickness: dynamics of the cavity evolution. Phys. Rev. 79 (3), 036306.

Berthelsen, P.A., Bachynski, E.E., et al., 2016. Real-time Hybrid Model Tests of a Braceless Semi-submersible Wind Turbine: Part III—Calibration of a Numerical Model. ASME 2016 35th International Conference on Ocean, Offshore and Arctic Engineering. American Society of Mechanical Engineers Digital Collection.

Brown, S.A., Magar, V., et al., 2014. An evaluation of RANS turbulence closure models for spilling breakers. Coastal Engineering Proceedings (34), 5-5.

Bruinsma, N., Paulsen, B., et al., 2018. Validation and application of a fully nonlinear numerical wave tank for simulating floating offshore wind turbines. Ocean. Eng. 147, 647–658.

Coulling, A.J., Goupee, A.J., et al., 2013. Importance of Second-Order Difference-Frequency Wave-Diffraction Forces in the Validation of a FAST Semi-submersible Floating Wind Turbine Model. No. NREL/CP-5000-57697. ASME 2013 32nd International Conference on Ocean, Offshore and Arctic Engineering. American Society of Mechanical Engineers Digital Collection.

Devolder, B., Rauwoens, P., et al., 2017. Application of a buoyancy-modified k-ω SST turbulence model to simulate wave run-up around a monopile subjected to regular waves using OpenFOAM®. Coast. Eng. 125, 81–94.

Dudley Brian, S., 1961. A single formula for the "law of the wall. J. Appl. Mech. 28 (3), 455–458.

Eça, L., Hoekstra, M., 2006. On the Influence of the Iterative Error in the Numerical Uncertainty of Ship Viscous Flow Calculations. 26th Symposium on Naval Hydrodynamics, Rome, Italy.

Eça, L., Hoekstra, M., 2014. A procedure for the estimation of the numerical uncertainty of CFD calculations based on grid refinement studies. J. Comput. Phys. 262, 104–130.

Fan, W., Anglart, H., 2020. varRhoTurbVOF: a new set of volume of fluid solvers for turbulent isothermal multiphase flows in OpenFOAM. Comput. Phys. Commun. 247, 106876.

Fonseca, N., Pessoa, J., et al., 2011. Experimental and numerical investigation of the slowly varying wave exciting drift forces on a restrained body in bi-chromatic waves. Ocean Eng. 38 (17–18), 2000–2014.

Hirt, C.W., Nichols, B.D., 1981. Volume of fluid (VOF) method for the dynamics of free boundaries. J. Comput. Phys. 39 (1), 201–225.

Hu, C., Sueyoshi, M., et al., 2014. Hydrodynamic Analysis of a Semi-submersible Type Floating Wind Turbine. The Eleventh ISOPE Pacific/Asia Offshore Mechanics Symposium. International Society of Offshore and Polar Engineers.

Jacobsen, N.G., Fuhrman, D.R., et al., 2012. A wave generation toolbox for the open-source CFD library: OpenFoam®. Int. J. Numer. Methods Fluid. 70 (9), 1073–1088.

Launder, B.E., Spalding, D.B., 1983. The Numerical Computation of Turbulent Flows. Numerical Prediction of Flow, Heat Transfer, Turbulence and Combustion. Elsevier, pp. 96–116.

Lee, C.-H., 1995. WAMIT Theory Manual. Massachusetts Institute of Technology, Department of Ocean Engineering.

Li, H., Bachynski, E.E., 2021. Experimental and numerical investigation of nonlinear diffraction wave loads on a semi-submersible wind turbine. Renew. Energy: Accepted for publication 171, 709–727.

Liu, C., Hu, C., 2014. CFD simulation of a floating wind turbine platform in rough sea conditions. In: The Twenty-Fourth International Ocean and Polar Engineering Conference. International Society of Offshore and Polar Engineers.

Lopez-Pavon, C., Watai, R.A., et al., 2015. Influence of wave induced second-order forces in semisubmersible fowt mooring design. J. Offshore Mech. Arctic Eng. 137 (3).

Luan, C., Gao, Z., et al., 2016. Design and Analysis of a Braceless Steel 5-MW Semi-submersible Wind Turbine. ASME 2016 35th International Conference on Ocean, Offshore and Arctic Engineering. American Society of Mechanical Engineers Digital Collection.

Madsen, P.A., Fuhrman, D.R., 2006. Third-order theory for bichromatic bi-directional water waves. J. Fluid Mech. 557, 369–397.

Marintek, 2012. SIMO—Theory Manual Version 4.0. Marintek Trondheim, Norway.

Marthinsen, T., Winterstein, S.R., 1992. On the skewness of random surface waves. In: The Second International Offshore and Polar Engineering Conference. International Society of Offshore and Polar Engineers.

Menter, F., Ferreira, J.C., et al., 2003. The SST turbulence model with improved wall treatment for heat transfer predictions in gas turbines. Proceedings of the international gas turbine congress 1, 2–7.

Menter, F.R., Kuntz, M., et al., 2003. Ten years of industrial experience with the SST turbulence model. Turbulence, heat and mass transfer 4 (1), 625–632.

Ohyama, T., Hsu, J.R., 1995. Nonlinear wave effect on the slow drift motion of a floating body. Appl. Ocean Res. 17 (6), 349–362.

Ormberg, H., Passano, E., 2012. RIFLEX Theory Manual. Marintek, Trondheim.

Pessoa, J., Fonseca, N., 2015. Second-order low-frequency drift motions of a floating body calculated by different approximation methods. J. Mar. Sci. Technol. 20 (2), 357–372.

Pessoa, J.o., Fonseca, N., et al., 2010. Experimental and Numerical Study of the Depth Effect on the First Order and Slowly Varying Motions of a Floating Body in Bichromatic Waves. International Conference on Offshore Mechanics and Arctic Engineering.

Rahman, M.M., Karim, M.M., et al., 2007. Numerical investigation of unsteady flow past a circular cylinder using 2-D finite volume method. J. Nav. Architect. Mar. Eng. 4 (1), 27–42.

Rivera-Arreba, I., Bruinsma, N., et al., 2019. Modeling of a semisubmersible floating offshore wind platform in severe waves. J. Offshore Mech. Arctic Eng. 141 (6).

Robertson, A., Bachynski, E.E., et al., 2020. Total experimental uncertainty in hydrodynamic testing of a semisubmersible wind turbine, considering numerical propagation of systematic uncertainty. Ocean. Eng. 195, 106605.

Robertson, A., Jonkman, J., et al., 2014a. Definition of the Semisubmersible Floating System for Phase II of OC4. No. NREL/TP-5000-60601. National Renewable Energy Lab.(NREL), Golden, CO (United States).

Robertson, A., Jonkman, J., et al., 2014b. Offshore Code Comparison Collaboration Continuation within IEA Wind Task 30: Phase II Results Regarding a Floating Semisubmersible Wind System. No. NREL/CP-5000-61154. ASME 2014 33rd International Conference on Ocean, Offshore and Arctic Engineering. American Society of Mechanical Engineers Digital Collection.

Robertson, A., Jonkman, J., et al., 2016. Definition of the OC5 DeepCwind Semisubmersible Floating System. Technical report NREL.

Robertson, A.N., Gueydon, S., et al., 2020. OC6 Phase I: Investigating the Under-prediction of Floating Wind Turbine Loads at Their Natural Frequencies. The Science of Making Torque from Wind (TORQUE 2020). National Renewable Energy Lab. (NREL), Golden, CO (United States).

Robertson, A.N., Wendt, F., et al., 2017. OC5 project phase II: validation of global loads of the DeepCwind floating semisubmersible wind turbine. Energy Procedia 137, 38–57.

Simos, A.N., Ruggeri, F., et al., 2018. Slow-drift of a floating wind turbine: an assessment of frequency-domain methods based on model tests. Renew. Energy 116, 133–154.

Tom, N., Robertson, A., et al., 2019. Bichromatic wave selection for validation of the difference-frequency transfer function for the OC6 validation campaign. In: International Conference on Offshore Mechanics and Arctic Engineering. American Society of Mechanical Engineers.

Wang, L., Robertson, A., et al., 2021. Investigation of nonlinear difference-frequency wave excitation on a semisubmersible offshore-wind platform with bichromatic-wave CFD simulations. In: Proceedings of the ASME 2020 3rd International Offshore Wind Techanical Conference. Boston, MA, USA.

Weller, H.G., Tabor, G., et al., 1998. A tensorial approach to computational continuum mechanics using object-oriented techniques. Comput. Phys. 12 (6), 620–631.

Wilcox, D.C., 1998. Turbulence Modeling for CFD. DCW industries La Canada, CA.